Voltage-controlled ferromagnetism and magnetoresistance in LaCoO3/SrTiO3 heterostructures

Chengqing Hu, Keun Woo Park, Agham Posadas, Jean L. Jordan-Sweet, Alexander A. Demkov et al.

Citation: J. Appl. Phys. **114**, 183909 (2013); doi: 10.1063/1.4831673
View online: http://dx.doi.org/10.1063/1.4831673
View Table of Contents: http://jap.aip.org/resource/1/JAPIAU/v114/i18
Published by the AIP Publishing LLC.

Voltage-controlled ferromagnetism and magnetoresistance in $LaCoO_3/SrTiO_3$ heterostructures

Chengqing Hu,[1] Keun Woo Park,[1] Agham Posadas,[2] Jean L. Jordan-Sweet,[3] Alexander A. Demkov,[2] and Edward T. Yu[1]
[1]*Microelectronics Research Center, The University of Texas at Austin, 10100 Burnet Rd., Austin, Texas 78758, USA*
[2]*Department of Physics, The University of Texas at Austin, 1 University Station C1600, Austin, Texas 78712, USA*
[3]*IBM Thomas J. Watson Research Center, Yorktown Heights, New York 10598, USA*

(Received 11 July 2013; accepted 31 October 2013; published online 13 November 2013)

A $LaCoO_3/SrTiO_3$ heterostructure grown on Si (001) is shown to provide electrically switchable ferromagnetism, a large, electrically tunable magnetoresistance, and a vehicle for achieving and probing electrical control over ferromagnetic behavior at submicron dimensions. Fabrication of devices in a field-effect transistor geometry enables application of a gate bias voltage that modulates strain in the heterostructure via the converse piezoelectric effect in $SrTiO_3$, leading to an artificial inverse magnetoelectric effect arising from the dependence of ferromagnetism in the $LaCoO_3$ layer on strain. Below the Curie temperature of the $LaCoO_3$ layer, this effect leads to modulation of resistance in $LaCoO_3$ as large as 100%, and magnetoresistance as high as 80%, both of which arise from carrier scattering at ferromagnetic-nonmagnetic interfaces in $LaCoO_3$. Finite-element numerical modeling of electric field distributions is used to explain the dependence of carrier transport behavior on gate contact geometry, and a Valet-Fert transport model enables determination of spin polarization in the $LaCoO_3$ layer. Piezoresponse force microscopy is used to confirm the existence of piezoelectric response in $SrTiO_3$ grown on Si (001). It is also shown that this structure offers the possibility of achieving exclusive-NOR logic functionality within a single device. © *2013 AIP Publishing LLC*. [http://dx.doi.org/10.1063/1.4831673]

I. INTRODUCTION

Complex oxide materials and heterostructures have excited tremendous interest in research due to the wealth of new physical phenomena they exhibit and their potential for producing solid-state device functionality unattainable with conventional semiconductor materials. In particular, multiferroic and other multifunctional oxide materials offer rich possibilities for exploration of both fundamental physical phenomena and device applications,[1–13] and with the advancement of thin film growth techniques for such oxide materials, epitaxial oxide heterostructures are emerging as outstanding candidates for realization of devices in which diverse material properties—ferromagnetism, piezoelectricity, ferroelectricity, and others—are flexibly coupled to achieve new functionality. Among various possibilities for combining electronic, magnetic, or other functionalities, electric-field control of magnetism has piqued particularly intense interest, and may provide an attractive alternative to approaches such as current-induced spin-transfer torque for low-power magnetization switching. Electric-field modulation of magnetization direction, saturation magnetization, or coercive field has previously been demonstrated,[14–38] as have switching between ferromagnetic and paramagnetic states via modulation of carrier concentration in itinerant magnetic materials, generally using a liquid electrolyte as a gate contact,[39–43] and macroscopic control over interfacial magnetocrystalline anisotropy in a multiferroic epitaxial heterostructure.[44,45] However, practical device structures making use of electric-field switching of ferromagnetism that remain amenable to on-chip integration with established Si and Si-based electronics and device size scaling are still lacking.

In this work, we have employed an approach that combines strain-dependent ferromagnetism in $LaCoO_3$ (Refs. 46–53) with piezoelectric response in $SrTiO_3$ (Refs. 20 and 54–57) in a single-crystal oxide heterostructure grown on Si (001) to enable application of a gate voltage in a suitably fabricated device to modulate strain in both the $SrTiO_3$ and $LaCoO_3$, and consequently ferromagnetism in the $LaCoO_3$ layer. Creation of spatially alternating ferromagnetic and nonmagnetic regions in a $LaCoO_3$ film in this manner leads to a voltage-dependent magnetoresistance,[58] and engineering of the strain distribution within the $LaCoO_3/SrTiO_3$ heterostructure enables realization of exclusive–NOR logic functionality within a single device. In addition, monolithic integration on Si (001) via epitaxial growth offers the possibility of incorporating these and related devices into mainstream Si-based nanoelectronic circuits and systems.

II. EXPERIMENT

The epitaxial layer structures employed in these studies were grown by molecular beam epitaxy (DCA M600) from elemental sources and consisted of 8 nm $SrTiO_3$ grown on a p-type Si.(001) ($\rho \sim 0.01\ \Omega$ cm) substrate, followed by 30 nm $LaCoO_3$.[47] Prior to growth, the Si substrates were degreased in acetone, isopropanol, and deionized water for 5 min each with sonication. The substrates were then exposed to ultraviolet/ozone for 15 min to volatilize hydrocarbon impurities.

After loading into the MBE chamber, the Si was outgassed for 10 min at 650 °C and the native SiO_2 layer was removed by Sr-assisted deoxidation.[59] $SrTiO_3$ was grown on Si using a ½ monolayer Sr template[60] with the metal fluxes adjusted to yield a total growth rate of 0.4 nm/min. The first 1.6 nm were grown at 200 °C and vacuum annealed at 550 °C for 5 min. The rest of the $SrTiO_3$ layer was grown at 550 °C to achieve a total thickness of 8 nm. $SrTiO_3$ growth was done using molecular oxygen as the oxidant at a partial pressure of 2×10^{-7} Torr. After $SrTiO_3$ growth, the substrate temperature was raised to 700 °C while the atomic oxygen rf plasma source power was being ramped up. $LaCoO_3$ was grown under atomic oxygen (rf power 300 W and oxygen background pressure of 1×10^{-5} Torr) at a growth rate of 0.6 nm/min to a total thickness of 30 nm. After growth, the sample was cooled in oxygen (1×10^{-5} Torr) at a rate of 10 °C/min down to room temperature. High temperature growth of the $LaCoO_3$ layer under atomic oxygen also results in the formation of ~8.5 nm SiO_2 between the Si and $SrTiO_3$, which relaxes compressive strain in $SrTiO_3$ on Si[61] and provides additional tensile strain in $LaCoO_3$ that helps stabilize ferromagnetism in that layer, and also isolates the active device region from the conducting Si substrate. Electrical contacts to the $LaCoO_3$ layer were formed by initial deposition of 25 nm SiO_2, followed by e-beam lithography and etching of 4 μm × 2.5 μm contact windows and deposition of Ti/Au contact metallization. The typical length of the $LaCoO_3$ channel formed in this manner was 13 μm for $M = 9$ and 26 μm for $M = 18$. For each device, two Ti/Au gate contacts were formed on the SiO_2 layer above the channel in an alternating finger pattern by e-beam lithography, e-beam evaporation, and lift-off. The finger widths for the two gate contacts are 500 nm and 200 nm, with adjacent fingers separated by 150 nm. A Carl Zeiss Neon 40 scanning electron microscope was used to obtain the images shown in Figure 1(b).

X-ray diffraction (XRD) was performed at the National Synchrotron Light Source beamline X20A using a high resolution triple-axis geometry with a Ge(111) monochromator and analyzer. The x-ray wavelength was 1.5407Å and the incident beam divergence was ~0.01°. Grazing incidence and reflection scans were measured for the determination of in-plane lattice parameters at an angle of $\alpha = \beta = 0.4°$ to the sample surface, along both the h00 and hk0 directions. Out-of-plane lattice parameters were measured from Bragg-Brentano scans through the 00l peaks. Rocking curves were also taken to determine the FWHM of epitaxial alignment.

All the electrical measurements were performed in a LakeShore EMPX-HF probe station with a high vacuum (10^{-6} mbar) chamber. Liquid nitrogen was used for low temperature measurements. An Agilent 4156A precision semiconductor parameter analyzer was used for applying a channel bias voltage and measuring electrical currents; an Agilent B2912A precision source/measure unit was used to apply a gate bias voltage. The temperature dependence of the $LaCoO_3$ resistivity was determined by using standard four-probe measurements in which one port from the Agilent B2912A precision source/measure unit was connected as a current source providing 1 nA–400 μA of current (depending on temperature) between the two end contacts of a standard four-contact device designed and fabricated specifically for four-probe measurements and the other port connected to the two middle contacts across which the voltage drop was measured. For magnetic field sweep measurements, the magnetic field was first swept from 0 Oe to +5 kOe (−5 kOe) with $V_{G1} = +15$ V, followed by resetting V_{G1} and H successively and then a second field sweep from 0 Oe to +5 kOe (−5 kOe).

The electrostatic module from Comsol Multiphysics was used for the finite element modeling and simulations. A gate bias voltage of 15 V was applied as a boundary condition at locations corresponding to the gate contacts. The Si substrate was assumed to form a conductive plane in the simulation since it was heavily doped. Relative dielectric constants used are 3.9 for SiO_2, 1000 for $LaCoO_3$ (estimated based on Huang *et al.*[62]) without considering the rather limited electric field screening effect, and 300 for $SrTiO_3$.[63,64]

The piezoresponse force microscopy (PFM) measurements were performed at room temperature using a Bruker ICON atomic force microscope system with a Co/Cr coated MESP-tip in contact mode. PFM images were obtained with 4.5 V amplitude, 8 kHz ac voltage modulation at 0 V dc bias and the setpoint was minimized to prevent excessive wearing

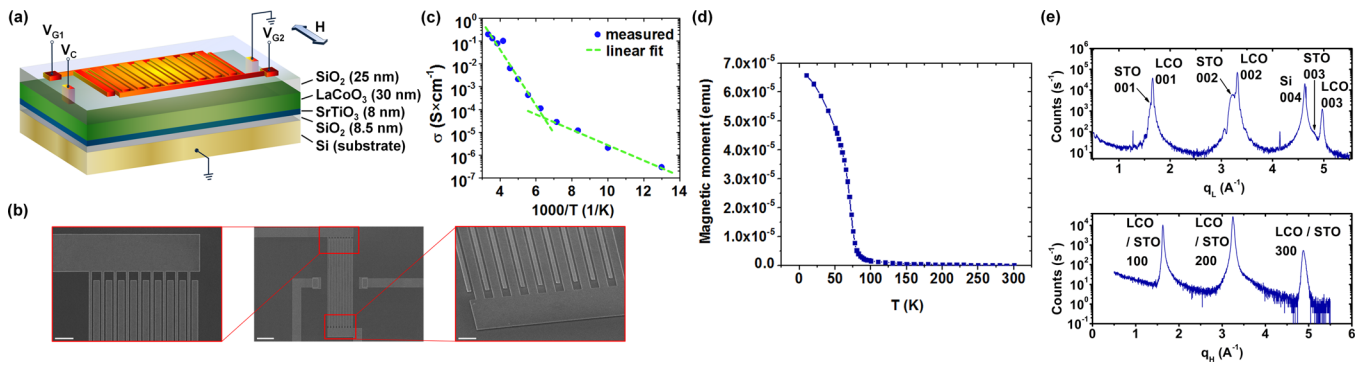

FIG. 1. (a) Schematic diagram of device structure, applied voltages, and external magnetic field geometry. (b) SEM images of device. Scale bars from left to right are 1.5 μm, 6 μm, and 1 μm, respectively. (c) Conductivity of the $LaCoO_3$ channel measured as a function of temperature ranging from 77 K to 300 K. Two distinct slopes are observed in different temperature ranges (77 K to 150 K and 150 K to 300 K) indicating two different regimes of electronic transport. (d) Magnetization of $LaCoO_3$ as a function of temperature at a constant magnetic field of 1 kOe under field-cooled conditions. The film is ferromagnetic with a Curie temperature of 85 K. (e) X-ray diffraction data of $LaCoO_3$ (30 nm)/$SrTiO_3$ (8 nm)/SiO_2 (8.5 nm)/Si. The $LaCoO_3$ peaks are indexed using the pseudocubic notation. The data show that $LaCoO_3$ and $SrTiO_3$ are coherently strained to each other, and they are indeed epitaxially grown on Si.

of the tip coating. The system has two lock-in amplifiers which detect the same frequency component of the four-quadrant photodiode detector as that of the applied electric field, one for the horizontal and the other for the vertical deflections.

III. RESULTS AND DISCUSSION

Figure 1(a) shows a schematic diagram of a completed device structure along with electrical contact and external field geometries, with scanning electron micrographs of a representative device structure shown in Figure 1(b). The 8.5 nm SiO_2 layer indicated in Figure 1(a) forms during the growth of $LaCoO_3$, which requires high temperature (700 °C) and the use of atomic oxygen from an oxygen plasma source. The oxidation of the Si after $SrTiO_3$ growth does not disrupt the crystalline structure of the $SrTiO_3$ layer away from the SiO_2, allowing for subsequent epitaxial growth of $LaCoO_3$,[61] and relieving strain induced by the Si substrate in the $SrTiO_3$. Minimal intermixing at the $LaCoO_3/SrTiO_3$ interface is expected under these conditions.[47] The basic device geometry is that of a field-effect transistor in which the $LaCoO_3$ layer acts as the transistor channel, with source-drain voltage V_C and dual gate contacts with voltages V_{G1} and V_{G2} applied.

Figure 1(c) shows temperature-dependent channel conductivity, measured using a standard four-probe method under zero external magnetic field. Two temperature regimes, 77 K–150 K and 150 K–300 K, both showing an Arrhenius or Arrhenius-like relation, can be seen with different activation energies, respectively, providing insight into the temperature-dependent electrical transport in thin-film single-crystal $LaCoO_3$. It is known that polaronic conduction plays an important role in electrical transport in many strongly correlated oxides. This has been observed for bulk $LaCoO_3$, in which small polarons are formed by mobile holes in the valence band due to electron thermal excitation whereas electrons are deeply trapped and therefore immobile.[65] The small-polaron motion is known to occur by two distinct mechanisms.[66,67] At low temperatures, the small polaron moves by Bloch-type band motion and the temperature dependence of the dc conductivity is given as $\sigma = e\mu_{\mathrm{low\,T}} n_0 \exp(-E_g/2k_BT)$, where e denotes the electronic charge, n_0 is the number of low-spin Co(III) sites per unit volume at very low temperatures, $\mu_{\mathrm{low\,T}}$ is the mobility of small-polarons at low temperatures slowly depending on T as for conventional semiconductors, and E_g is the quasi-constant band gap of $LaCoO_3$. In this regime, the small-polaron transport can be described in a conventional way widely used for most semiconductors. At high temperatures, however, thermally activated phonon-induced small-polaron hopping dominates and the conductivity-temperature relation is expressed as $\sigma T = A_0 \exp\left[-\left(W_H + E_g/2\right)/k_BT\right]$, where A_0 is a constant, W_H is the hopping energy of a polaron, and the small-polaron hopping mobility is exponentially depending on $1/T$. The $\sigma - T$ data obtained in our work for the $LaCoO_3$ thin film are in accord with this theory, from which E_g and W_H are estimated to be 0.14 eV and 0.19 eV, respectively, close to those reported by Iguchi *et al.*[65] Therefore, as described below, the Valet-Fert model derived from the Boltzmann equation can be used to describe electrical transport in the $LaCoO_3$ film at temperatures below 150 K.[58]

The magnetic properties of the $LaCoO_3$ were measured using a Quantum Design superconducting quantum interference device (SQUID) magnetometer. The magnetization as a function of temperature from 300 K to 10 K was measured under an applied field of 1 kOe in a field-cooled condition, after the film was first saturated at 10 K under a field of 40 kOe. The field was applied in the plane of the film. Figure 1(d) shows the ferromagnetic transition temperature of 85 K for the strained $LaCoO_3$ in our study. The $LaCoO_3$ film was also characterized using XRD to determine the lattice constants and overall crystalline quality (Figure 1(e) and Figure S1). The c lattice constants of the $LaCoO_3$ layer and the underlying $SrTiO_3$ layer are determined to be 3.79 Å and 3.91 Å, respectively, whereas the a (in-plane) lattice constants of the two layers are both 3.87 Å, consistent with biaxially tensile-strained $LaCoO_3$ with an in-plane lattice constant identical to that of the $SrTiO_3$. Excellent crystalline quality of the $LaCoO_3$ layer as well as the $SrTiO_3$ layer is evident from both Figure 1(e) and the results of the transmission electron microscopy as well as the x-ray photoelectron spectroscopy measurements of the same structure.[47] The observation of coherent strain in $LaCoO_3$ thin films at such a large thickness (30 nm) has also been reported by Fuchs *et al.*[68] and is known to be anomalously large compared to the expected critical thickness from the Blakeslee formula. This has been attributed to the existence of nanotwins in $LaCoO_3$ that accommodate the strain without elastic relaxation.

Figures 2(a) and 2(b) show channel current I measured as a function of V_C for different gate voltages V_{G1}, at 300 K and 77 K, respectively, with $V_{G2} = 0$ V and an external magnetic field of 4.5 kOe applied in all cases. The I-V_C curves are nonlinear throughout the entire channel bias range, indicating the presence of Schottky contacts to the $LaCoO_3$ channel and leading to a contact resistance that is voltage dependent. I is seen to be independent of V_{G1} at 300 K, but to be strongly suppressed for $V_{G1} = +15$ V at 77 K. Furthermore, a +15 V bias was applied to either set of gate fingers with 0 V channel bias at 77 K, and the measured current at either end of the channel was smaller than 50 pA (not shown), so the possibility of any contribution by a gate leakage current to the observed current suppression can be eliminated. We can define a normalized resistance change,

$$\Delta R/R_0 \equiv \left(R|_{V_{G1}} - R|_{V_{G1}=0}\right)/R|_{V_{G1}=0}, \quad (1)$$

as a function of V_{G1}, where $R \equiv V_C/I$ is the channel resistance. Here, R contains both the total contact resistance R_c and the $LaCoO_3$ channel resistance R_{channel}. To compare and analyze R_{channel} under different conditions, we use a fixed channel voltage $V_C = 8$ V, in which case R_c is fixed and relatively small, and makes a negligible contribution to the resistance change. Figure 2(c) shows $\Delta R/R_0$ as a function of temperature for $V_{G1} = -15$ V and $V_{G1} = +15$ V, with $V_C = 8$ V in all cases. For $V_{G1} = +15$ V, there is a sharp drop in $\Delta R/R_0$ between 80 K and 90 K, with negligible dependence on temperature observed above 100 K. This transition

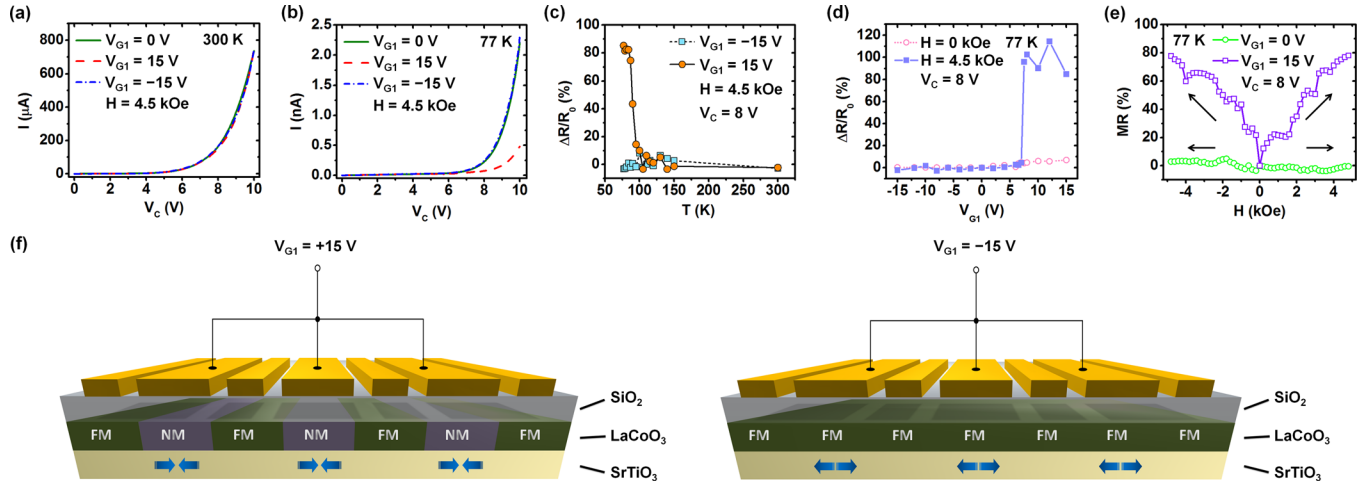

FIG. 2. (a) Channel current I vs. channel voltage V_C at 300 K with $H = 4.5$ kOe for gate voltages $V_{G1} = -15$ V, 0 V, and +15 V. V_{G1} is seen to have no effect on channel current flow. (b) Channel current vs. V_C at 77 K with $H = 4.5$ kOe for $V_{G1} = -15$ V, 0 V, and +15 V. Channel current is strongly suppressed for $V_{G1} = +15$ V. (c) $\Delta R/R_0$ vs. T for $V_C = 8$ V and $H = 4.5$ kOe at $V_{G1} = +15$ V and $V_{G1} = -15$ V. Nonzero $\Delta R/R_0$ is observed only for $V_{G1} = +15$ V, and only below the Curie temperature of the $LaCoO_3$ layer. (d) $\Delta R/R_0$ vs. V_{G1} for $V_C = 8$ V at 77 K with/without an external magnetic field H. Negligible change in resistance is observed in the absence of an external magnetic field. For $H = 4.5$ kOe, an abrupt transition in $\Delta R/R_0$ is observed at $V_{G1} = 7.5$ V. (e) MR vs. external magnetic field H for $V_C = 8$ V at 77 K, and gate bias voltages $V_{G1} = 0$ V, +15 V. Magnetic field was first swept from 0 Oe to +5 kOe (−5 kOe) with $V_{G1} = +15$ V, followed by resetting V_{G1} and H successively and then a second field sweep from 0 Oe to +5 kOe (−5 kOe). (f) Illustration of the postulated materials response to $V_{G1} = +15$ V and −15 V, respectively. $V_{G1} = +15$ V results in lateral compression of the $SrTiO_3$ layer below the fingers followed by a ferromagnetic-nonmagnetic transition of $LaCoO_3$ in these regions, whereas $V_{G1} = -15$ V increases tensile strain in the $SrTiO_3$ layer and the $LaCoO_3$ layer atop remains ferromagnetic.

coincides in temperature with the measured Curie temperature of strained $LaCoO_3$ of ~85 K,[47] suggesting a connection between the electrical behavior shown in Figures 2(b) and 2(c) and ferromagnetism in the $LaCoO_3$ layer. Further evidence suggesting such a connection can be seen in Figure 2(d), which shows $\Delta R/R_0$ as a function of V_{G1} at 77 K for $V_C = 8$ V and external magnetic fields of 0 and 4.5 kOe. (see supplementary material, Figure S2, for the full dependence of I on V_C and V_{G1}.[69]) Two features are of particular interest. First, no dependence of channel resistance on V_{G1} is observed in the absence of an applied magnetic field, indicating that magnetic-field-dependent transport plays a significant role. Second, in the presence of an external magnetic field, the channel resistance increases very abruptly at $V_{G1} = 7.5$ V, indicative of an abrupt change in magnetotransport behavior at that voltage. We define magnetoresistance in the channel of the device to be given by

$$MR \equiv \left(R|_H - R|_{H=0}\right)/R|_{H=0}, \tag{2}$$

where R is again the channel resistance and H is the external magnetic field. Figure 2(e) shows magnetoresistance as a function of external magnetic field for $V_{G1} = 0$ and 15 V. Nonzero magnetoresistance is observed only for $V_{G1} = 15$ V, and increases to values as high as 80% for an external field of 5 kOe. We also fabricated a device with a uniform planar gate structure, but for reasons described below $\Delta R/R_0$ and MR were both found to be zero for this device.

The mechanism we propose as being responsible for the observed electrical behavior is illustrated schematically in Figure 2(f). Application of a gate voltage V_{G1} modulates strain in the $SrTiO_3$ layer through the existence of a piezoelectric response, specifically the converse piezoelectric effect in which the electric field produced by V_{G1} leads to mechanical deformation of the $SrTiO_3$. The resulting strain field extends into the adjacent $LaCoO_3$ layer, allowing the strain in that layer to be modulated by the gate voltage as well. Because a critical minimum level of tensile strain is required to induce ferromagnetism in the $LaCoO_3$ layer,[47,49] varying V_{G1} allows strain in the $LaCoO_3$ layer to be modulated across the critical level required to induce the transition to ferromagnetic behavior, enabling electrical control of ferromagnetism in $LaCoO_3$ to be achieved. As previously reported,[49] ferromagnetism occurs in the $LaCoO_3$ layer above a threshold value of tensile strain; for lower strain values, the $LaCoO_3$ is nonmagnetic. The XRD data shown in Figure 1(e) suggest that the tensile strain of $LaCoO_3$ without gate bias is in the vicinity of this critical point, so that modulation of ferromagnetism of the $LaCoO_3$ would require an in-plane strain change of order ~0.1%. The dependence of channel resistance on gate voltage and magnetic field then arises as a consequence of spatially dependent modulation of ferromagnetism in the $LaCoO_3$ channel due to the geometry of the gate contacts, and increased carrier scattering at ferromagnet-nonmagnet interfaces within the channel. It should be noted that screening of the gate electric field by the thin $LaCoO_3$ layer is weak due to the low carrier density in that layer at low temperatures (e.g., 77 K), and therefore most of the electric field under a sufficient gate bias (e.g., 15 V) still enters the $SrTiO_3$ layer beneath.

Key to this mechanism is the existence of piezoelectric response in the $SrTiO_3$ layer. Figure 3 shows results of PFM[70] measurements performed on a $LaCoO_3$(30 nm)/$SrTiO_3$(8 nm) heterostructure grown on Si (001). Room-temperature piezoelectric response, which in our $SrTiO_3$ layers can be stabilized by compressive strain[55–57] imposed by the upper $LaCoO_3$ layer, is clearly visible in images of both amplitude (Figure 3(b)) and phase (Figure 3(c)), and the statistical distribution of

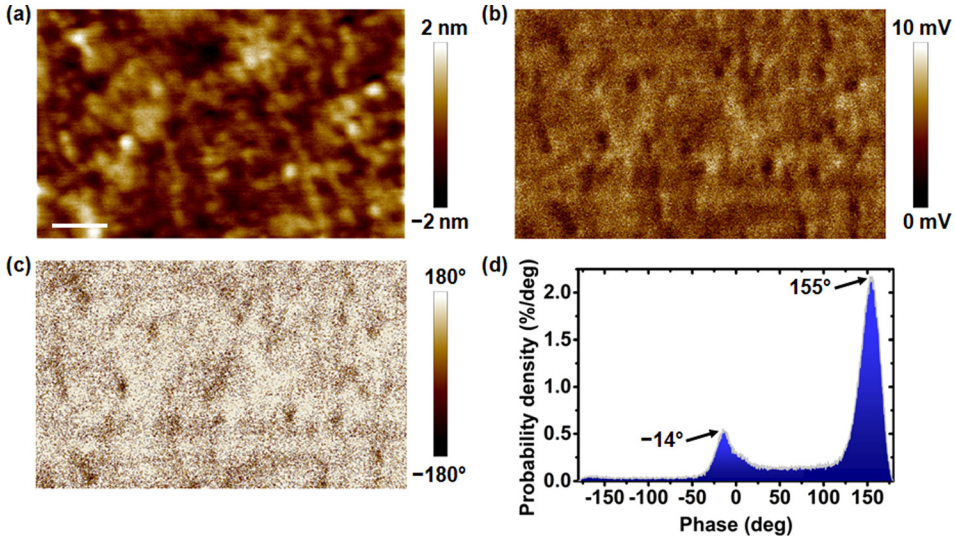

FIG. 3. (a) Surface topography. Scale bar is 150 nm. (b) PFM lateral amplitude image. (c) PFM lateral phase image. (d) PFM lateral phase histogram. Nonzero signal in the PFM amplitude image confirms the existence of piezoelectric response in the structure, while the histogram showing a bimodal phase response distribution indicates the presence of one dominant orientation for piezoelectric response, and the existence of smaller regions with inverted orientation.

PFM phase response shown in Figure 3(d) unambiguously indicates the existence of a dominant material polarity, verifying the poled nature of the piezoelectric $SrTiO_3$ layer and consistent with the observation that only a positive gate voltage (above a threshold) results in current suppression. While the PFM measurements shown here were performed at room temperature, earlier studies have indicated that piezoelectricity in $SrTiO_3$ can be maintained and, indeed, increase at low temperature.[54] Similar measurements were performed on samples in which the $SrTiO_3$ layer was replaced by MBE-grown heavily La-doped highly conductive $SrTiO_3$ in which sufficient carriers are activated from the La doping level and the electric field across the $SrTiO_3$ layer would be dramatically reduced or eliminated due to free carrier screening; no PFM response was observed, indicating that the piezoelectric response shown in Figure 3 arises from $SrTiO_3$ rather than $LaCoO_3$.

Investigation of the influence of gate finger geometry provides further insight into the roles of strain, strain-dependent ferromagnetism, and ferromagnet-nonmagnet interface scattering on electronic transport characteristics. Figure 4(a) shows a cross-sectional schematic of the device geometry illustrated in Figure 1, with two sets of interdigitated gate fingers of length (in the direction of channel current transport) 500 nm and 200 nm separated by gaps of 150 nm between adjacent fingers, to which voltages V_{G1} and V_{G2}, respectively, are applied. Figure 4(b) shows channel current, measured at 77 K with $H = 4.5$ kOe, as a function of V_C for different gate voltage configurations. High channel current is observed for $V_{G1} = V_{G2} = 0$ V, while much lower current is observed when +15 V is applied to one, but not both, sets of gate fingers–consistent with the influence of ferromagnet-nonmagnet interface scattering that arises when regions of nonmagnetic material are created by application of positive voltage to one set of gate fingers. However, high current flow is observed for $V_{G1} = V_{G2} = +15$ V. The origin of this ostensibly counterintuitive observation is revealed in Figure 4(c), which shows a finite-element numerical simulation of the vertical component of electric field within the device region indicated by the dashed line in Figure 4(a) for different gate voltage configurations. Note that the simulated vertical electric field in the $SrTiO_3$ layer is approximate since the dielectric constant used for $SrTiO_3$ in the simulation is assumed to be $300\varepsilon_0$, which is for strain-free $SrTiO_3$ at room temperature and not necessarily applicable to piezoelectric strained $SrTiO_3$ thin films.[57] Nevertheless, the electric field distribution profile elucidated by the simulation is qualitatively correct, and sufficient to illustrate the key points in our discussion. For $V_{G1} = V_{G2} = 0$ V (not shown), no electric field, and consequently no strain modulation arising from the converse piezoelectric effect, is present. When either V_{G1} or V_{G2} (but not both) is increased to +15 V, there is a strong modulation of the electric field, and consequently strain, along the length of the channel, resulting in alternating regions of ferromagnetic and nonmagnetic $LaCoO_3$ in the channel. The resulting interface scattering leads to reduced channel current, as seen experimentally in Figure 4(b). For $V_{G1} = V_{G2} = +15$ V, however, the spacing between adjacent gate fingers is sufficiently small that the fringing fields at the edge of each gate finger yield much weaker variation in electric field, and consequently strain, along the length of the channel. As a result, the transition from ferromagnetic to nonmagnetic behavior occurs throughout the channel, resulting in high channel current due to the absence of interfacial scattering except at the ends of the channel region. We also note that this behavior further excludes the conventional MOSFET working mechanism as being responsible for the observed effect and, more interestingly, allows the device to provide exclusive-NOR logic functionality, as illustrated in Figure 4(d).

An analysis based on the Valet-Fert model[58] for current transport in magnetic and nonmagnetic multilayers provides both insight into factors dominating current transport in these devices, and quantitative estimates of spin polarization in the $LaCoO_3$ layer (see supplementary material for detailed derivations and discussions[69]). Applicability of the Valet-Fert model to describe electrical transport in the $LaCoO_3$ film at 77 K can be confirmed from the conductivity data shown in Figure 1(c). As discussed above, the small-polaron transport in the $LaCoO_3$ film at temperatures below 150 K is Bloch-type band motion, analogous to carrier transport in conventional semiconductors with a large effective mass, to which the Boltzmann transport equation is applicable.[66]

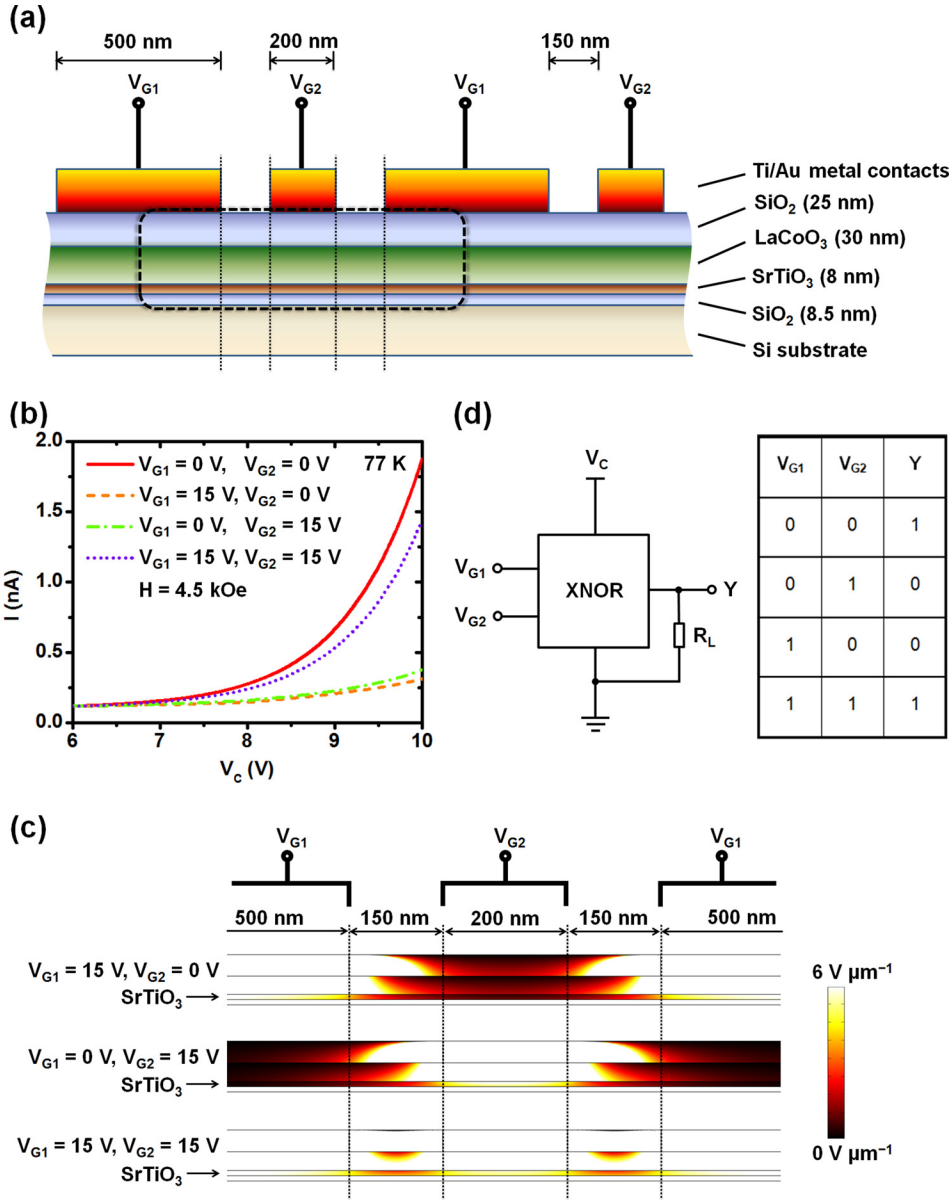

V_{G1}	V_{G2}	Y
0	0	1
0	1	0
1	0	0
1	1	1

FIG. 4. (a) Cross-sectional view of device geometry and contact configuration for finite-element modeling of electric field distribution. Simulation results of the circumscribed region are shown in (c). (b) Channel current vs. V_C at 77 K with $H = 4.5$ kOe for (i) $V_{G1} = 0$ V, $V_{G2} = 0$ V; (ii) $V_{G1} = +15$ V, $V_{G2} = 0$ V; (iii) $V_{G1} = 0$ V, $V_{G2} = +15$ V; and (iv). $V_{G1} = +15$ V, $V_{G2} = +15$ V. Different gate biasing configurations lead to different electric field distributions and therefore variations in modulation of strain in the $SrTiO_3$ layer, and of ferromagnetism in the $LaCoO_3$ layer. (c) Finite element simulations of electric field (vertical component) distributions in the $SrTiO_3$ layer for gate voltage applied in different configurations. In the first two cases where +15 V is applied to either set of gate fingers, well-defined unbiased regions in the $SrTiO_3$ layer can be found. In the third case, fringing fields at the gate contact edges penetrate the unbiased region, leading to laterally extended modulation in electric field and consequently strain. This expansion in electric field modulation results in reduced modulation of channel current in the case of $V_{G1} = V_{G2} = +15$ V. (d) Schematic diagram (left) and truth table (right) for a two-input exclusive-NOR (XNOR) logic gate implemented by our device structure. High (low) voltage is defined as 1 (0) for both inputs and output so that $Y = V_{G1} \odot V_{G2}$.

Valet and Fert[58] derived macroscopic transport equations, i.e., the Valet-Fert model, starting from the Boltzmann equation and formally justified its validity in the limit that the spin-diffusion length of each material is long compared to the mean free path of the same material, regardless of the layer thicknesses. This approach was further proved to be accurate for spin-diffusion lengths comparable to the mean free paths both theoretically by numerical studies of the Boltzmann equation[71] and experimentally.[72] In our device structure, the minimum length of each ferromagnetic or nonmagnetic region is 200 nm, which is expected to be much larger than the mean free path in the $LaCoO_3$ layer given the large effective mass and consequently low mobility in the small-polaron narrow band. Therefore, the Valet-Fert model can be safely used to describe electrical transport in the $LaCoO_3$ layer at low temperatures (77 K–150 K). Figure 5 shows schematic illustrations of the primary factors contributing to the resistance of the $LaCoO_3$ channel in the presence (Figure 5(a)) and absence (Figure 5(b)) of nonmagnetic regions within the ferromagnetic $LaCoO_3$. In Figure 5(a), alternating ferromagnetic and nonmagnetic regions of length t_F and t_N, respectively, have areal resistance $(1-\beta^2)\rho_F{}^*t_F$ and $\rho_N{}^*t_N$, where β is the spin polarization in the ferromagnetic $LaCoO_3$ layer, and $\rho_F{}^*$ and $\rho_N{}^*$ are the resistivity of the ferromagnetic and nonmagnetic segments. These segments are separated by interfacial regions of areal resistance $(1-\gamma^2)r_b{}^*$, where γ is the spin polarization at the interface and $r_b{}^*$ the interfacial resistance. In Figure 5(b), the entire channel is ferromagnetic and the resistance of a single period L is given by $(1-\beta^2)\rho_F{}^*L$. To estimate the spin polarization β in $LaCoO_3$, we note that the resistance change $\Delta R/R_0$ and magnetoresistance MR, defined in Eqs. (1) and (2), respectively, can be related to each other according to the expression

$$MR = (1-\beta^2)\Delta R/R_0 - \beta^2. \quad (3)$$

Using values for MR and $\Delta R/R_0$ from Figure 2 for $H = 4.5$ kOe, $V_C = 8$ V, and $V_{G1} = 15$ V at 77 K, we obtain $\beta = 0.24 \pm 0.02$. An independent estimate of β can be obtained from a comparison of values for $\Delta R/R_0$ obtained using

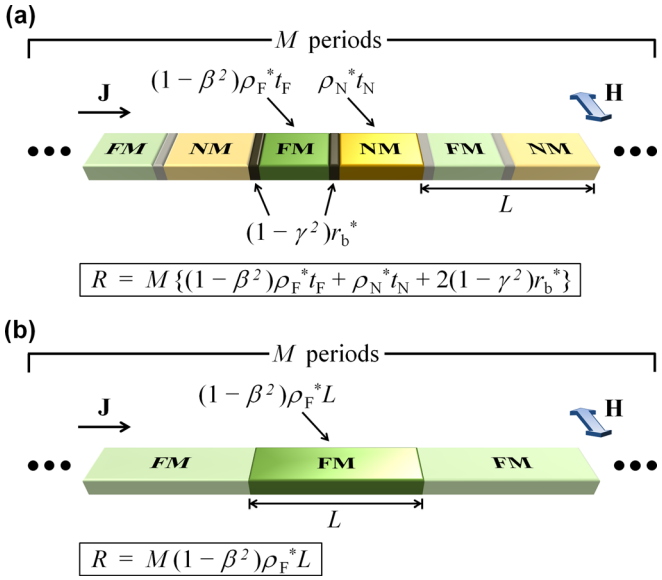

FIG. 5. (a) The Valet-Fert current channel model for the case of $V_G > V_{th}$. β and γ are bulk spin polarization in ferromagnetic $LaCoO_3$ and interfacial spin polarization at the interface between ferromagnetic $LaCoO_3$ and nonmagnetic $LaCoO_3$, respectively. Both ρ_F^* and ρ_N^* are resistivities of the $LaCoO_3$ channel at 77 K, L is the length of the channel for one period within which t_F (t_N) is length of the ferromagnetic (nonmagnetic) channel, and M is the total number of periods in the channel. Nonmagnetic regions form and lead to nonzero magnetic domain wall resistances at the interface with ferromagnetic regions so that three terms, i.e., $(1-\beta^2)\rho_F^* t_F$ from ferromagnetic $LaCoO_3$, $\rho_N^* t_N$ from nonmagnetic $LaCoO_3$, and $2(1-\gamma^2)r_b^*$ from magnetic domain walls, contribute to the total channel resistance R. b) The Valet-Fert model for $V_G < V_{th}$. The entire channel is ferromagnetic and domain wall resistance is absent, in which case only one term $(1-\beta^2)\rho_F^* L$ contributes to R.

different gate dimensions, as in Figure 4(b). This approach yields $\beta = 0.29 \pm 0.01$, in very good agreement with that obtained from Eq. (3). Equation (3) also implies that *MR* should be independent of the number of periods, M, of the interdigitated finger structure, and therefore of the number of ferromagnet-nonmagnet interfaces traversed. It should be noted that since a magnetic field of 5 kOe is not sufficient to saturate the magnetization of our $LaCoO_3$ film,[47] the spin polarization β extracted at 5 kOe is not the spin polarization of a magnetically saturated $LaCoO_3$ layer. The extracted spin polarization in this work, however, is still useful in validating our use of the Valet-Fert model, and more importantly, the method described to extract the spin polarization should be applicable in magnetically saturated films as well. Table I shows measured values of *MR* for device structures with different gate dimensions and number of periods M, along with *MR* values predicted by Eq. (3) using values of $\Delta R/R_0$ measured using the same devices and spin polarization $\beta = 0.27 \pm 0.03$. As predicted, *MR* is seen to be independent of M, and to vary as expected with $\Delta R/R_0$ for different gate dimensions. As discussed in more detail in supplementary material,[69] the value of β obtained above together with the fact that no distinguishable resistance change was observed by applying a positive voltage to a planar gate uniformly over the entire channel further indicates that the magnetic domain wall scattering at ferromagnetic-nonmagnetic interfaces rather than the difference in conductivity of the ferromagnetic and nonmagnetic phase predominantly leads to the large $\Delta R/R_0$ and *MR*. As a thought experiment, it might seem surprising that $(1-\beta^2)\rho_F^* t_F$ vanishes as β approaches 1, yielding a negative resistance change when ferromagnetic-nonmagnetic interfaces form. However, as discussed in supplementary material,[69] the resistance due to interfacial scattering would increase with β, still leading to positive $\Delta R/R_0$ and *MR*.

TABLE I. Measured and calculated *MR* at $V_C = 8$ V, $T = 77$ K, and $H = 4.5$ kOe for different gate biasing configurations and number of periods in a single device. Excellent consistency between measured *MR* data and corresponding values calculated using the Valet-Fert model, particularly the fact that *MR* is independent of M, strongly supports the basic applicability of the Valet-Fert model and the role of ferromagnet-nonmagnet interface scattering in the experimental observation.

M	9		18
V_{G1} (V)	15	0	15
V_{G2} (V)	0	15	0
MR_{meas} (%)	75.0 ± 0.5	71.0 ± 0.8	75.7 ± 0.6
MR_{cal} (%)	71.8 ± 3.0	68.7 ± 3.0	72.3 ± 3.1

IV. SUMMARY

In summary, we have designed, characterized, and analyzed devices based on $LaCoO_3/SrTiO_3$ heterostructures grown on Si (001) substrates by MBE in which the combination of strain-dependent ferromagnetism in $LaCoO_3$, the converse piezoelectric effect in $SrTiO_3$, and strain coupling between these layers enables electrically controlled ferromagnetism and magnetoresistance to be achieved. Detailed mechanisms explaining this behavior are developed and verified using (i) the Valet-Fert model to quantify $LaCoO_3$ spin polarization, magnetic interfacial resistances, and the dependence of magnetoresistance on device geometry; (ii) finite-element modeling of electric field distributions to explain variations in current transport for different gate finger geometries; and (iii) PFM studies to confirm the presence of piezoelectric response in $SrTiO_3$ films within our device structures. These results illustrate a new approach for electrically controlling local ferromagnetism in complex oxide heterostructures and for probing and controlling spin transport behavior in complex oxides at submicron dimensions, and offer the possibility of straightforward integration with conventional Si-based electronics via epitaxial growth directly on Si substrates.

ACKNOWLEDGMENTS

We thank Hosung Seo and Leonard F. Register for fruitful discussions. Use of the National Synchrotron Light Source, Brookhaven National Laboratory, was supported by the U.S. Department of Energy, Office of Science, Office of Basic Energy Sciences, under Contract No. DE-AC02-98CH10886. Part of this work was supported by the National Science Foundation (DMR-0548182, DMR-1006725, and DMR-1066430), the Office of Naval Research (N000 14-10-1-0489), and the Judson S. Swearingen Regents Chair in Engineering at The University of Texas at Austin.

[1]H. Y. Hwang, Y. Iwasa, M. Kawasaki, B. Keimer, N. Nagaosa, and Y. Tokura, Nature Mater. **11**, 103–113 (2012).

[2]J. Mannhart and D. G. Schlom, Science **327**, 1607–1611 (2010).
[3]M. Bibes, J. E. Villegas, and A. Barthélémy, Adv. Phys. **60**, 5–84 (2011).
[4]P. Zubko, S. Gariglio, M. Gabay, P. Ghosez, and J.-M. Triscone, Annu. Rev. Condens. Matter Phys. **2**, 141–165 (2011).
[5]J. M. Rondinelli and N. A. Spaldin, Adv. Mater. **23**, 3363–3381 (2011).
[6]C. H. Ahn, J.–M. Triscone, and J. Mannhart, Nature **424**, 1015–1018 (2003).
[7]P. Moetakef, J. R. Williams, D. G. Ouellette, A. P. Kajdos, D. Goldhaber-Gordon, S. J. Allen, and S. Stemmer, Phys. Rev. X **2**, 021014 (2012).
[8]Y. Xie, C. Bell, Y. Hikita, and H. Y. Hwang, Adv. Mater. **23**, 1744–1747 (2011).
[9]W. Eerenstein, N. D. Mathur, and J. F. Scott, Nature **442**, 759–765 (2006).
[10]S.-W. Cheong and M. Mostovoy, Nature Mater. **6**, 13–20 (2007).
[11]R. Ramesh and N. A. Spaldin, Nature Mater. **6**, 21–29 (2007).
[12]C. A. F. Vaz, J. Hoffman, C. H. Ahn, and R. Ramesh, Adv. Mater. **22**, 2900–2918 (2010).
[13]L. W. Martin, S. P. Crane, Y.-H. Chu, M. B. Holcomb, M. Gajek, M. Huijben, C.-H. Yang, N. Balke, and R. Ramesh, J. Phys.: Condens. Matter **20**, 434220 (2008).
[14]J. Wang, J. B. Neaton, H. Zheng, V. Nagarajan, S. B. Ogale, B. Liu, D. Viehland, V. Vaithyanathan, D. G. Schlom, U. V. Waghmare, N. A. Spaldin, K. M. Rabe, M. Wuttig, and R. Ramesh, Science **299**, 1719–1722 (2003).
[15]T. Zhao, A. Scholl, F. Zavaliche, K. Lee, M. Barry, A. Doran, M. P. Cruz, Y. H. Chu, C. Ederer, N. A. Spaldin, R. R. Das, D. M. Kim, S. H. Baek, C. B. Eom, and R. Ramesh, Nature Mater. **5**, 823–829 (2006).
[16]I. C. Infante, J. Juraszek, S. Fusil, B. Dupé, P. Gemeiner, O. Diéguez, F. Pailloux, S. Jouen, E. Jacquet, G. Geneste, J. Pacaud, J. Íñiguez, L. Bellaiche, A. Barthélémy, B. Dkhil, and M. Bibes, Phys. Rev. Lett. **107**, 237601 (2011).
[17]M. Ramazanoglu, M. Laver, W. Ratcliff II, S. M. Watson, W. C. Chen, A. Jackson, K. Kothapalli, S. Lee, S.-W. Cheong, and V. Kiryukhin, Phys. Rev. Lett. **107**, 207206 (2011).
[18]N. Balke, S. Choudhury, S. Jesse, M. Huijben, Y. H. Chu, A. P. Baddorf, L. Q. Chen, R. Ramesh, and S. V. Kalinin, Nat. Nanotechnol. **4**, 868–875 (2009).
[19]S. H. Baek, H. W. Jang, C. M. Folkman, Y. L. Li, B. Winchester, J. X. Zhang, Q. He, Y. H. Chu, C. T. Nelson, M. S. Rzchowski, X. Q. Pan, R. Ramesh, L. Q. Chen, and C. B. Eom, Nature Mater. **9**, 309–314 (2010).
[20]A. Vasudevarao, A. Kumar, L. Tian, J. H. Haeni, Y. L. Li, C.-J. Eklund, Q. X. Jia, R. Uecker, P. Reiche, K. M. Rabe, L. Q. Chen, D. G. Schlom, and V. Gopalan, Phys. Rev. Lett. **97**, 257602 (2006).
[21]M. Gajek, M. Bibes, S. Fusil, K. Bouzehouane, J. Fontcuberta, A. Barthélémy, and A. Fert, Nature Mater. **6**, 296–302 (2007).
[22]W.-G. Wang, M. Li, S. Hageman, and C. L. Chien, Nature Mater. **11**, 64–68 (2011).
[23]D. Chiba, M. Sawicki, Y. Nishitani, Y. Nakatani, F. Matsukura, and H. Ohno, Nature **455**, 515–518 (2008).
[24]J. T. Heron, M. Trassin, K. Ashraf, M. Gajek, Q. He, S. Y. Yang, D. E. Nikonov, Y.-H. Chu, S. Salahuddin, and R. Ramesh, Phys. Rev. Lett. **107**, 217202 (2011).
[25]L. W. Martin, Y.-H. Chu, M. B. Holcomb, M. Huijben, P. Yu, S.-J. Han, D. Lee, S. X. Wang, and R. Ramesh, Nano Lett. **8**, 2050–2055 (2008).
[26]J. Allibe, S. Fusil, K. Bouzehouane, C. Daumont, D. Sando, E. Jacquet, C. Deranlot, M. Bibes, and A. Barthélémy, Nano Lett. **12**, 1141–1145 (2012).
[27]H. Zheng, J. Wang, S. E. Lofland, Z. Ma, L. Mohaddes-Ardabili, T. Zhao, L. Salamanca-Riba, S. R. Shinde, S. B. Ogale, F. Bai, D. Viehland, Y. Jia, D. G. Schlom, M. Wuttig, A. Roytburd, and R. Ramesh, Science **303**, 661–663 (2004).
[28]F. Zavaliche, H. Zheng, L. Mohaddes-Ardabili, S. Y. Yang, Q. Zhan, P. Shafer, E. Reilly, R. Chopdekar, Y. Jia, P. Wright, D. G. Schlom, Y. Suzuki, and R. Ramesh, Nano Lett. **5**, 1793–1796 (2005).
[29]S. Zhang, Y. G. Zhao, P. S. Li, J. J. Yang, S. Rizwan, J. X. Zhang, J. Seidel, T. L. Qu, Y. J. Yang, Z. L. Luo, Q. He, T. Zou, Q. P. Chen, J. W. Wang, L. F. Yang, Y. Sun, Y. Z. Wu, X. Xiao, X. F. Jin, J. Huang, C. Gao, X. F. Han, and R. Ramesh, Phys. Rev. Lett. **108**, 137203 (2012).
[30]Y.-H. Chu, L. W. Martin, M. B. Holcomb, M. Gajek, S.-J. Han, Q. He, N. Balke, C.-H. Yang, D. Lee, W. Hu, Q. Zhan, P.-L. Yang, A. Fraile-Rodríguez, A. Scholl, S. X. Wang, and R. Ramesh, Nature Mater. **7**, 478–482 (2008).
[31]M. Liu, O. Obi, J. Lou, Y. Chen, Z. Cai, S. Stoute, M. Espanol, M. Lew, X. Situ, K. S. Ziemer, V. G. Harris, and N. X. Sun, Adv. Funct. Mater. **19**, 1826–1831 (2009).
[32]J. Lou, M. Liu, D. Reed, Y. Ren, and N. X. Sun, Adv. Mater. **21**, 4711–4715 (2009).
[33]X. Hong, A. Posadas, A. Lin, and C. H. Ahn, Phys. Rev. B **68**, 134415 (2003).
[34]C. A. F. Vaz, Y. Segal, J. Hoffman, R. D. Grober, F. J. Walker, and C. H. Ahn, Appl. Phys. Lett. **97**, 042506 (2010).
[35]H. J. A. Molegraaf, J. Hoffman, C. A. F. Vaz, S. Gariglio, D. van der Marel, C. H. Ahn, and J.-M. Triscone, Adv. Mater. **21**, 3470–3474 (2009).
[36]S. Valencia, A. Crassous, L. Bocher, V. Garcia, X. Moya, R. O. Cherifi, C. Deranlot, K. Bouzehouane, S. Fusil, A. Zobelli, A. Gloter, N. D. Mathur, A. Gaupp, R. Abrudan, F. Radu, A. Barthélémy, and M. Bibes, Nature Mater. **10**, 753–758 (2011).
[37]L. Bocher, A. Gloter, A. Crassous, V. Garcia, K. March, A. Zobelli, S. Valencia, S. Enouz-Vedrenne, X. Moya, N. D. Marthur, C. Deranlot, S. Fusil, K. Bouzehouane, M. Bibes, A. Barthélémy, C. Colliex, and O. Stéphan, Nano Lett. **12**, 376–382 (2012).
[38]C. A. F. Vaz, J. Phys.: Condens. Matter **24**, 333201 (2012).
[39]M. Weisheit, S. Fähler, A. Marty, Y. Souche, C. Poinsignon, and D. Givord, Science **315**, 349 (2007).
[40]H. Ohno, D. Chiba, F. Matsukura, T. Omiya, E. Abe, T. Dietl, Y. Ohno, and K. Ohtani, Nature **408**, 944–946 (2000).
[41]D. Chiba, M. Yamanouchi, F. Matsukura, and H. Ohno, Science **301**, 943–945 (2003).
[42]D. Chiba, S. Fukami, K. Shimamura, N. Ishiwata, K. Kobayashi, and T. Ono, Nature Mater. **10**, 853–856 (2011).
[43]Y. Yamada, K. Ueno, T. Fukumura, H. T. Yuan, H. Shimotani, Y. Iwasa, L. Gu, S. Tsukimoto, Y. Ikuhara, and M. Kawasaki, Science **332**, 1065 (2011).
[44]W. Eerenstein, M. Wiora, J. L. Prieto, J. F. Scott, and N. D. Mathur, Nature Mater. **6**, 348–351 (2007).
[45]J. D. Burton and E. Y. Tsymbal, Phys. Rev. B **80**, 174406 (2009).
[46]D. Fuchs, C. Pinta, T. Schwarz, P. Schweiss, P. Nagel, S. Schuppler, R. Schneider, M. Merz, G. Roth, and H. v. Löhneysen, Phys. Rev. B **75**, 144402 (2007).
[47]A. Posadas, M. Berg, H. Seo, A. de Lozanne, A. A. Demkov, D. J. Smith, A. P. Kirk, D. Zhernokletov, and R. M. Wallace, Appl. Phys. Lett. **98**, 053104 (2011).
[48]G. E. Sterbinsky, P. J. Ryan, J.-W. Kim, E. Karapetrova, J. X. Ma, J. Shi, and J. C. Woicik, Phys. Rev. B **85**, 020403(R) (2012).
[49]H. Seo, A. Posadas, and A. A. Demkov, Phys. Rev. B **86**, 014430 (2012).
[50]D. Fuchs, E. Arac, C. Pinta, S. Schuppler, R. Schneider, and H. v. Löhneysen, Phys. Rev. B **77**, 014434 (2008).
[51]A. Herklotz, A. D. Rata, L. Schultz, and K. Dörr, Phys. Rev. B **79**, 092409 (2009).
[52]K. Dörr, O. Bilani-Zeneli, A. Herklotz, A. D. Rata, K. Boldyreva, J.-W. Kim, M. C. Dekker, K. Nenkov, L. Schultz, and M. Reibold, Eur. Phys. J. B **71**, 361–366 (2009).
[53]S. Park, P. Ryan, E. Karapetrova, J. W. Kim, J. X. Ma, J. Shi, J. W. Freeland, and W. Wu, Appl. Phys. Lett. **95**, 072508 (2009).
[54]D. E. Grupp and A. M. Goldman, Science **276**, 392 (1997).
[55]J. H. Haeni, P. Irvin, W. Chang, R. Uecker, P. Reiche, Y. L. Li, S. Choudhury, W. Tian, M. E. Hawley, B. Craigo, A. K. Tagantsev, X. Q. Pan, S. K. Streiffer, L. Q. Chen, S. W. Kirchoefer, J. Levy, and D. G. Schlom, Nature **430**, 758–761 (2004).
[56]M. P. Warusawithana, C. Cen, C. R. Sleasman, J. C. Woicik, Y. Li, L. F. Kourkoutis, J. A. Klug, H. Li, P. Ryan, L.-P. Wang, M. Bedzyk, D. A. Muller, L.-Q. Chen, J. Levy, and D. G. Schlom, Science **324**, 367–370 (2009).
[57]H. W. Jang, A. Kumar, S. Denev, M. D. Biegalski, P. Maksymovych, C. W. Bark, C. T. Nelson, C. M. Folkman, S. H. Baek, N. Balke, C. M. Brooks, D. A. Tenne, D. G. Schlom, L. Q. Chen, X. Q. Pan, S. V. Kalinin, V. Gopalan, and C. B. Eom, Phys. Rev. Lett. **104**, 197601 (2010).
[58]T. Valet and A. Fert, Phys. Rev. B **48**, 7099–7113 (1993).
[59]Y. Wei, X. Hu, Y. Liang, D. C. Jordan, B. Craigo, R. Droopad, Z. Yu, A. Demkov, J. L. Edwards, and W. J. Ooms, J. Vac. Sci. Technol. B **20**, 1402 (2002).
[60]A. A. Demkov and X. Zhang, J. Appl. Phys. **103**, 103710 (2008).
[61]M. Choi, A. Posadas, R. Dargis, C.-K. Shih, A. A. Demkov, D. H. Triyoso, N. D. Theodore, C. Dubourdieu, J. Bruley, and J. Jordan-Sweet, J. Appl. Phys. **111**, 064112 (2012).
[62]T.-W. Huang, Y.-S. Chang, G.-J. Chen, C.-C. Chung, and Y.-H. Chang, J. Electrochem. Soc. **154**, G244–G250 (2007).
[63]D. Fuchs, C. W. Schneider, R. Schneider, and H. Rietschel, J. Appl. Phys. **85**, 7362 (1999).

[64]M. L. Reinle-Schmitt, C. Cancellieri, D. Li, D. Fontaine, M. Medarde, E. Pomjakushina, C. W. Schneider, S. Gariglio, Ph. Ghosez, J.-M. Triscone, and P. R. Willmott, Nat. Commun. **3**, 932 (2012).
[65]E. Iguchi, K. Ueda, and W. H. Jung, Phys. Rev. B **54**, 17431–17437 (1996).
[66]J. T. Devreese, Ency. Appl. Phys. **14**, 383–409 (1996).
[67]I. K. Naik and T. Y. Tien, J. Phys. Chem. Solids **39**, 311–315 (1978).
[68]D. Fuchs, L. Dieterle, E. Arac, R. Eder, P. Adelmann, V. Eyert, T. Kopp, R. Schneider, D. Gerthsen, and H. v. Löhneysen, Phys. Rev. B **79**, 024424 (2009).
[69]See supplementary material at http://dx.doi.org/10.1063/1.4831673 for more information on the XRD data, *I-V* characteristics, and detailed derivation of the model used for spin polarization and transport analysis.
[70]A. Gruverman, O. Auciello, and H. Tokumoto, Annu. Rev. Mater. Sci. **28**, 101–123 (1998).
[71]D. R. Penn and M. D. Stiles, Phys. Rev. B **72**, 212410 (2005).
[72]J. Bass, W. P. Pratt, and P. A. Schroeder, Comments Condens. Matter Phys. **18**, 223 (1998).